Proceedings of the Reactor Physics Asia 2015 (RPHA15) Conference
Jeju, Korea, Sept. 16-18, 2015

Discrete Ordinates Methods with Curved Spatial Grids : an Alternative Method to MOC

Changyuan Liu[a,*], and Edward Larsen[a]
[a]*Department of Nuclear Engineering and Radiological Sciences,*
University of Michigan, Ann Arbor, MI, 48109, USA
[*]Corresponding author: changyuan_liu@163.com

1. Introduction

The method of characteristic (MOC) has been favored for many recent whole core transport codes; some current research codes are: the nTRACER code [4] from Seoul National University, the MPACT code [11] from the University of Michigan, and the Dragon code [9] from École Polytechnique de Montréal. However, it is well-known that whole core transport with MOC is both computational expensive and requires significant storage. On the other hand, the discrete ordinates (SN) methods have been successfully applied to large systems, as done demonstrated by the computer code Attila. [8]

However, all previous discrete-ordinates methods implemented in available production computer codes were formulated only for problems containing spatial cells with planar boundaries. This creates geometric approximations and inefficiencies for modeling any physical system with curved boundaries – the curved boundaries must be approximated using a greatly many very fine spatial cells, each fine cell having a planar boundary. Fig. 1. illustrates what's new in this paper.

In this paper, we derive, implement, and test 2-D discrete-ordinates methods, which are applicable for systems having curved interfaces between material regions, and which treat these curved surfaces analytically. The key benefits of discrete-ordinates methods on curved spatial grids over the MOC method include: (i) a standard highly-optimized quadrature sets, (ii) a single user-specified spatial grid, (iii) a simple extension to 3-D transport, and (iv) a small memory footprint for the computer.

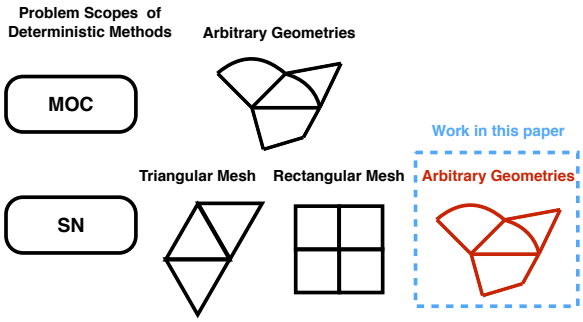

Fig. 1. The scope of the work in this paper [6]

2. Geometry & Topology

When SN methods are applied to curved spatial grids, the geometry is more complex than geometries with linear boundaries. The description of SN equations requires the "topology" information, which is a math term to represent the connectivity and neighborhoods information. So this section introduces the necessary terminology for later explanation of our SN methods.

2.1 Curve parametrization

We consider spatial grids that consist of any planar shapes bounded by lines and circular arcs or any other curve that can be parametrized. Although our method is not restricted to lines and circular arcs, we discuss only lines and circular arcs as examples. A curve is parametrized by associating all points on it with real numbers. A line and a circular arc are parametrized as:

$$\text{Line}: \quad \vec{x} = \vec{o} + t\,\hat{d},\ |\hat{d}| = 1,\ a \le t \le b, \quad (1)$$

$$\text{Circular Arc}: \quad \vec{x} = \vec{c} + r \begin{pmatrix} \cos t \\ \sin t \end{pmatrix},\ a \le t \le b, \quad (2)$$

where t is the parametrization parameter. If we "walk" along the curved in the direction of increasing parameter, the normal vector pointing to the "right" is defined as the "outer normal vector", which is denoted as $\hat{n}(t)$ for the point associating with parameter t. Fig. 2 illustrates this.

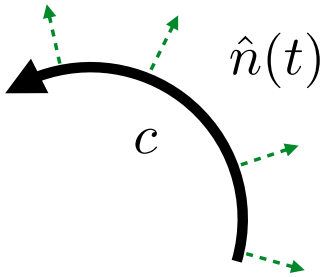

Fig. 2. The outer normal vector of the curve c at parameter t.

Next, several one-dimensional curve integrals for a curve c with parameter range $[a,b]$ are defined:

$$A_0(c) = \int_a^b dt, \quad (3)$$

$$A_{1x}(c) = \int_a^b n_x(t)dt, \quad (4)$$

$$A_{1y}(c) = \int_a^b n_y(t)dt, \quad (5)$$

$$\vec{A}_1(c) = \int_a^b \begin{pmatrix} n_x(t) \\ n_y(t) \end{pmatrix} dt = \begin{pmatrix} A_{1x}(c) \\ A_{1y}(c) \end{pmatrix}, \quad (6)$$

where $n_x(t)$ and $n_y(t)$ are respectively the x and y components of the outer normal vector $\hat{n}(t)$.

2.2 Topology

The geometry formed by lines and circular arcs can be much complex. Fig. 3. is an example shape formed by two circles and one triangle, which divide the space into 7 spatial "cells" with curved boundaries.

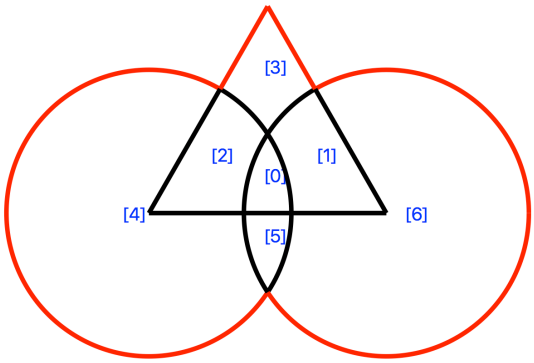

Fig. 3. Geometry formed by two circles and one triangle. The spatial "cell 1" is bounded by two lines and two circular arcs. The red lines denote the outer boundaries.

Consider a spatial cell f, all its boundaries are oriented are denoted as:

$$C(f) = \{c | c \text{ is a boundary of cell } f\}. \quad (7)$$

It is important to keep in mind that the boundaries are in the counter-clockwise direction. When two spatial cells share a common curved boundary, the common boundary has opposite directions for the two neighbor cells. Fig. 4. illustrates this.

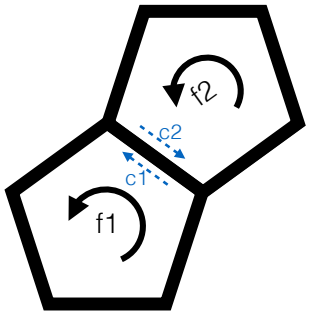

Fig. 4. Two cells and their boundaries. Two boundaries *c1* and *c2* have opposite directions when belonging to two neighboring cells *f1* and *f2*.

By divergence theorem, the sum of all boundary vector $\vec{A}_1$, as defined in equation (6), is zero for a spatial cell:

$$\sum_{c \in C(f)} \vec{A}_1(c) = 0. \quad (8)$$

Furthermore, we define a volume integral over the spatial cell *f*:

$$M_0(f) = \text{area of spatial cell } f. \quad (9)$$

3. Neutron Balance Equation

The SN algorithm is derived from integration of the neutron transport equation over a spacial cell. This section derives one important equation called the **neutron balance equation**, which illustrates the balance of neutron population within a spacial cell.

3.1 Integration of neutron transport equation

Consider a spatial cell *f*, the integration of multigroup discrete ordinates equation with isotropic scattering is:

$$\begin{aligned} &\int_f \vec{\nabla} \cdot \hat{\Omega}_n \psi_{n,g}(\vec{x}) d\vec{x} \\ &+ \int_f \Sigma_{t,g}(\vec{x}) \psi_{n,g}(\vec{x}) d\vec{x} \\ &= \frac{1}{4\pi} \sum_{g'=1}^{G} \int_f \Sigma_{s,g' \to g}(\vec{x}) \phi_{g'}(\vec{x}) d\vec{x} \\ &+ \frac{1}{4\pi k} \sum_{g'=1}^{G} \int_f \chi_g(\vec{x}) \nu\Sigma_{f,g'}(\vec{x}) \phi_{g'}(\vec{x}) d\vec{x}, \end{aligned} \quad (10)$$

where *f* denotes the area of integration and $d\vec{x} = dxdy$; *n* is the angle index with a total number of *N* angle, and *g* is the energy group index with a total number of *G* energy groups; *k* is the reactivity coefficient or the eigenvalue of the equation; $\Sigma_{t,g}$ is the total cross section of group *g*, $\Sigma_{s,g' \to g}$ is the isotropic scattering cross section from group *g'* to group *g*, $\nu\Sigma_{f,g}$ is the fission yield cross section of group *g*, and χ_g is the fission spectrum of group *g*; $\hat{\Omega}_n$ is the unit vector of the direction of flight with angle index *n* and ω_n is the corresponding weight; $\psi_{n,g}$ is the angular flux at angle $\hat{\Omega}_n$ and group *g*, and ϕ_g is the scalar flux of group *g*. The angular flux and scalar flux are related with:

$$\phi_g(\vec{x}) = \sum_{n=1}^{N} \omega_n \psi_{n,g}(\vec{x}). \quad (11)$$

Recall equation (6) and equation (9) of the definition of boundary and area integrals, we define the following averaged boundary and area flux:

$$\psi_{n,g,c} = \frac{\hat{\Omega}_n \cdot \int_{a(c)}^{b(c)} \hat{n}(t) \psi_{n,g}(\vec{x}(t)) dt}{\hat{\Omega}_n \cdot \vec{A}_1(c)}, \quad (12)$$

$$\phi_{g,c} = \frac{\hat{\Omega}_n \cdot \int_{a(c)}^{b(c)} \hat{n}(t)\phi_g(\vec{x}(t))dt}{\hat{\Omega}_n \cdot \vec{A}_1(c)}, \quad (13)$$

$$\bar{\psi}_{n,g,f} = \frac{\int_f \psi_{n,g}(\vec{x})d\vec{x}}{M_0(f)}, \quad (14)$$

$$\bar{\phi}_{g,f} = \frac{\int_f \phi_g(\vec{x})d\vec{x}}{M_0(f)}, \quad (15)$$

where f denotes the spatial cell, and c denotes the boundary curve; $a(c)$ and $b(c)$ are the starting and ending parameter of the boundary curve. We further assume that the material is homogeneous within a spatial cell f : $\Sigma_{t,g,f}$ is the total cross section of group g; $\Sigma_{s,g'\to g,f}$ is the scattering cross section from group g' to group g; $\nu\Sigma_{f,g,f}$ is the fission yield cross section of group g; $\chi_{g,f}$ is the fission spectrum of group g. Then the integral neutron transport equation (10) becomes:

$$\begin{aligned}&\sum_{c\in C(f)} \hat{\Omega}_n \cdot \vec{A}_1(c)\psi_{n,g,c} \\ &+\Sigma_{t,g,f}M_0(f)\bar{\psi}_{n,g,f} \\ &= \frac{1}{4\pi}\sum_{g'=1}^{G}\Sigma_{s,g'\to g,f}M_0(f)\bar{\phi}_{g',f} \\ &+\frac{1}{4\pi k}\sum_{g'=1}^{G}\nu\Sigma_{f,g',f}M_0(f)\bar{\phi}_{g',f}.\end{aligned} \quad (16)$$

Furthermore, we define some source terms:

$$\bar{Q}_{s,g,f} = \frac{1}{4\pi}\sum_{g'=1}^{G}\Sigma_{s,g'\to g,f}\bar{\phi}_{g',f}, \quad (17)$$

$$\bar{Q}_{f,g,f} = \frac{1}{4\pi}\chi_{g,f}\sum_{g'=1}^{G}\nu\Sigma_{f,g',f}\bar{\phi}_{g',f}, \quad (18)$$

$$Q_{s,g,c} = \frac{1}{4\pi}\sum_{g'=1}^{G}\Sigma_{s,g'\to g,f}\phi_{g',c}, \quad (19)$$

$$Q_{f,g,c} = \frac{1}{4\pi}\chi_{g,f}\sum_{g'=1}^{G}\nu\Sigma_{f,g',f}\phi_{g',c}. \quad (20)$$

Then equation (16) becomes the **neutron balance equation:**

$$\begin{aligned}&\sum_{c\in C(f)} \hat{\Omega}_n \cdot \vec{A}_1(c)\psi_{n,g,c} \\ &+\Sigma_{t,g,f}M_0(f)\bar{\psi}_{n,g,f} \\ &= M_0(f)\left[\bar{Q}_{s,g,f} + \frac{1}{k}\bar{Q}_{f,g,f}\right].\end{aligned} \quad (21)$$

The unknowns in the neutron balance equation are the average boundary flux $\psi_{n,g,c}$ and the average area flux $\bar{\psi}_{n,g,f}$. We need more equations for solving these unknowns, and the additional equations are called **auxiliary equation**. By the process of source iteration, the source terms $\bar{Q}_{s,g,f}$ and $\bar{Q}_{f,g,f}$ are considered as known quantities.

4. Categorization of Boundaries

For a specific direction of flight, all boundaries of a spatial cell is defined as **incoming-like, outgoing-like,** or **parallel** based on the sign of the dot product between the **average outer normal vector** and the direction of flight. The average out normal vector for the boundary curve *c* is defined as:

$$\frac{\int_{a(c)}^{b(c)} \hat{n}(t)dt}{\int_{a(c)}^{b(c)} dt}, \quad (22)$$

which has the same direction with $\vec{A}_1(c)$, as defined in equation (6). Fig. 5. illustrates the categorization criterion.

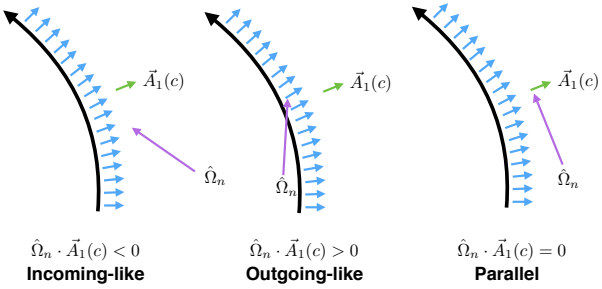

Fig. 5. Criterion of categorization of boundaries.

This categorizes all boundaries of a spatial cell f into three distinct sets:

$$C_{in}(f,\hat{\Omega}_n) = \{c \in C(f) \mid \vec{A}_1(c)\cdot\hat{\Omega}_n < 0\}, \quad (23)$$

$$C_{out}(f,\hat{\Omega}_n) = \{c \in C(f) \mid \vec{A}_1(c)\cdot\hat{\Omega}_n > 0\}, \quad (24)$$

$$C_{para}(f,\hat{\Omega}_n) = \{c \in C(f) \mid \vec{A}_1(c)\cdot\hat{\Omega}_n = 0\}. \quad (25)$$

For a curved boundary, even though it can have neutrons entering and exiting at the same time, the use of a single average outer normal vector or the $\vec{A}_1(c)$ vector categorize all boundaries without ambiguity. It is possible to split the spatial cell to avoid re-entering boundaries, but numerical results show that doing this gain little advantage. [6]

5. Auxiliary Equations

In section 3, we have derived one equation for the unknown average cell flux $\bar{\psi}_{n,g,f}$ and average boundary flux $\psi_{n,g,c}$. So additional equations are necessary. In

this section, we introduce 3 methods for derivation of additional **auxiliary equations**. All these auxiliary equations have only $\bar{\psi}_{n,g,f}$ and $\psi_{n,g,c}$ as the unknowns. By a process called **Sweeping** (introduced in section 6), the incoming boundary-averaged fluxes can be treated as known quantities.

5.1 Step method (STEP)

The assumption made in the **step method** is that the outgoing boundary-averaged fluxes equal the cell-averaged flux. So the step auxiliary equations are:

$$\psi_{n,g,c} = \bar{\psi}_{n,g,f}, \quad c \in C_{out}(f, \hat{\Omega}_n). \tag{26}$$

5.2 Simplified step characteristic method (SSC)

The assumption made in the **simplified step characteristics** method is that the neutron transport inside a spatial cell can be approximated by a 1-D transport along the direction of flight, as depicted in Fig. 6.

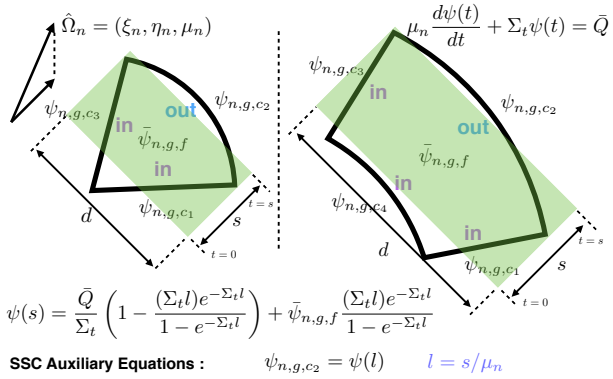

Fig. 6. Visualization of the SSC method

The SSC auxiliary equation is:

$$\begin{aligned} \psi_{n,g,c} &= \frac{\bar{Q}}{\Sigma_t}\left(1 - \frac{(\Sigma_t l)e^{-\Sigma_t l}}{1-e^{-\Sigma_t l}}\right) \\ &+ \bar{\psi}_{n,g,f}\frac{(\Sigma_t l)e^{-\Sigma_t l}}{1-e^{-\Sigma_t l}}, \\ & c \in C_{out}(f, \hat{\Omega}_n), \end{aligned} \tag{27}$$

where $\bar{Q}$ is the cell source density:

$$\bar{Q} = \bar{Q}_{s,g,f} + \frac{1}{k}\bar{Q}_{f,g,f}, \tag{28}$$

Σ_t is the cell total cross section:

$$\Sigma_t = \Sigma_{t,g,f}, \tag{29}$$

and l is the 1-D characteristic length in 3-D space:

$$l = s/\mu_n. \tag{30}$$

5.3 Multiple balance method (MB)

The auxiliary equations in the step and the SSC method contain no neutron physics. So it is more favorable if the auxiliary equations have forms similar to the neutron balance equation (21). In 1990, Morel & Larsen [10] have invented the **multiple balance** method for 1-D problem, in which the auxiliary equations have a form similar to the balance equation. To extend the method into 2-D, we define for each outgoing-like boundary c a weight function $w_c(\vec{x})$:

$$w_c(\vec{x}) = \alpha(c)\vec{A}_1(c)\cdot\vec{x} + \beta(c), \tag{31}$$

$$\forall\ \vec{x} \in \text{ cell } f\ :\ 0 \le w_c(\vec{x}) \le 1, \tag{32}$$

$$\exists\ \vec{x}_0 \in \text{ cell } f\ :\ w_c(\vec{x}_0) = 0, \tag{33}$$

$$\exists\ \vec{x}_0 \in \text{ boundary } c\ :\ w_c(\vec{x}_0) = 1. \tag{34}$$

The weight function has steepest sloop along the $\vec{A}_1(c)$ vector (see equation (7) for definition), and the coefficients $\alpha(c)$ and $\beta(c)$ are a function of the curve c, and are determined by the conditions given by the equations (32), (33) and (34).

The MB auxiliary equations are obtained by integrating the SN equation (10) with weight function $w_c(\vec{x})$ for each boundary c. The resultant MB auxiliary equation is:

$$\begin{aligned} &\hat{\Omega}_n \cdot \sum_{d\in C(f)} \left[\alpha(c)\begin{pmatrix} A_{1x}(c)A_{2xx}(d) + A_{1y}(c)A_{2xy}(d) \\ A_{1x}(c)A_{2yx}(d) + A_{1y}(c)A_{2yy}(d) \end{pmatrix}\right. \\ &\left. + \beta(c)\begin{pmatrix} A_{1x}(d) \\ A_{1y}(d) \end{pmatrix}\right](\psi_{n,g,d} - \bar{\psi}_{n,g,f}) \\ &+ [\alpha(c)(A_{1x}(c)M_{1x}(f) + A_{1y}(c)M_{1y}(f)) \\ &+ \beta(c)M_0(f)]\,\Sigma_{t,g,f}\psi_{n,g,c} \\ &= [\alpha(c)(A_{1x}(c)M_{1x}(f) + A_{1y}(c)M_{1y}(f)) \\ &+ \beta(c)M_0(f)]\left[Q_{s,g,c} + \frac{1}{k}Q_{f,g,c}\right], \end{aligned} \tag{35}$$

where the additional curve integrals are defined as:

$$A_{2xx}(c) = \int_{a(c)}^{b(c)} n_x(t)x(t)dt, \tag{36}$$

$$A_{2xy}(c) = \int_{a(c)}^{b(c)} n_x(t)y(t)dt, \tag{37}$$

$$A_{2yx}(c) = \int_{a(c)}^{b(c)} n_y(t)x(t)dt, \tag{38}$$

$$A_{2yy}(c) = \int_{a(c)}^{b(c)} n_y(t)y(t)dt, \tag{39}$$

and the additional cell integrals are defined as:

$$M_{1x}(f) = \int_f x d\vec{x}, \tag{40}$$

$$M_{1y}(f) = \int_f y d\vec{x}. \tag{42}$$

6. Sweep Algorithm

A 2-D curved spatial grid contains many spatial cells with curved boundaries. Each spatial cell is visited exactly once, and during each visit the cell's average cell flux and outgoing flux are updated according to the neutron balance equation (see section 3) and the auxiliary equations (see section 5). The order of visit is called the **sweep order**. To find the sweep order, an order graph is constructed, which requires that a cell is visited after all its **incoming-like** boundary-averaged flux are calculated. Section 4 discusses whether a boundary is **incoming-like**, **outgoing-like**, or **parallel** in details. Fig. 7. shows the sweep order and the order graph for a pin-cell.

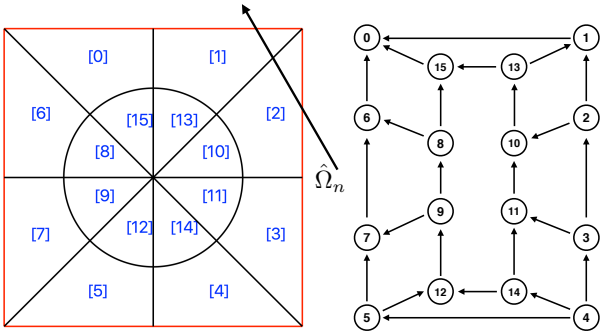

Fig. 7. Sweep order and order graph for a pin-cell.

7. WIMS-D Cross Section Library

To compare the SN methods and the widely used MOC method, the CASL VERA benchmark problems [1] are used. Because the benchmark document does not provide the cross section data, we use the WIMS-D library [5] to construct the macroscopic cross sections.

Table I. WIMS-D Material Composition for VERA Problems

Material	WIMS ID	Atomic Density #/barn-cm
Fuel (3.1wt% UO2)		
U-234	234	6.11864E-06
U-235	2235	7.18132E-04
U-236	236	3.29861E-06
U-238	8238	2.21546E-02
O-16	6016	4.57642E-02
IFBA		
B-10	10	2.16410E-02
B-11	11	1.96824E-02
Zr	91	2.06616E-02
Moderator		
O-16	6016	2.48112E-02
H-1	3001	4.96224E-02
B-10	10	1.07070E-05
B-11	11	4.30971E-05
Gap		
He	4	2.68714E-05
Clad (Zircaloy-4)		
Zr	91	6.4439E+00
Sn	118	9.5120E-02
Fe	2056	1.3776E-02
Cr	52	6.5600E-03
Hf-176	2176	3.4014E-05
Hf-177	2177	1.2096E-04
Hf-178	2178	1.7841E-04
Hf-179	2179	8.9580E-05
Hf-180	2180	2.3201E-04

For resonant nuclide, the absorption and fission yield cross sections are calculated by the formula provided by the WIMS-D library document [5]:

$$\sigma_a(\sigma_b, T) = \frac{I_a(\sigma_b, T)}{1 - I_a(\sigma_b, T)/\sigma_b}, \tag{43}$$

$$\nu\sigma_f(\sigma_b, T) = \frac{I_f(\sigma_b, T)}{1 - I_a(\sigma_b, T)/\sigma_b}, \tag{44}$$

where I_a and I_f are absorption and fission resonance integrals, which are function of the background cross section σ_b and temperature T. The definition of the background cross section can be found in the WIMS-D document as well [5]. We ignore the self-shielding effects from the material heterogeneity [7], which causes significant error in the solution. However, because the purpose of this paper is to demonstrate that SN methods can be an alternative to the MOC method, high precision in multigroup cross section is not the goal here.

8. VERA Benchmark Problem

To compare the SN methods with the MOC method, the VERA benchmark problem 1A, 1E and 2A are studied here. Problem 1A is a single fuel pin-cell with no IFBA coating; problem 1E is a single fuel pin-cell with IFBA coating; problem 2A is a fuel assembly containing 17x17 pin-cells.

The multigroup Monte Carlo (MC) provides the reference solutions to different SN and MOC methods. Since we use the same cross section for the MC, SN, MOC methods, the errors in the solution are due to methods' accuracy only. Again, our purpose is not to validate our cross sections, but to demonstrate that SN

methods can be an alternative to MOC method. The MOC quadrature sets are denoted as "AmPn Dd", which means we use *m* azimuthal angles per quadrant, and *n* polar angles per octant, and a ray spacing of *d* cm. The SN quadrature sets are standard ones [3].

Table II. Number of angles in different quadrature sets

Quadrature Set	Number of Angles
MOC Quadrature Set	
A4P2	64
A4P4	128
A8P4	256
SN Quadrature Set	
S4	24
S8	80
S12	168
S16	288
S20	440

To compare the quality of the solution, we measure the collision rate, which is defined as:

$$CR = \sum_{g=1}^{G} \Sigma_{t,g} \bar{\phi}_g. \tag{45}$$

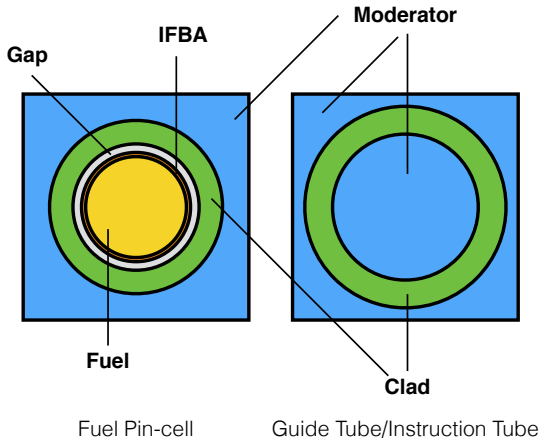

Fig. 8. The geometry for pin-cell [1]

Table III. Pin-cell Dimension Information [1]

Dimension	Value (cm)
Pitch (Size of Square)	1.26
Fuel Pin-cell (F)	
Outer radius of fuel	0.4096
Outer radius of IFBA	0.4106
Outer radius of gap	0.418
Outer radius of clad	0.475
Guide Tube Pin-cell (GT)	
Inner radius of clad	0.559
Outer radius of clad	0.605
Instruction Tube Pin-cell (IT)	
Inner radius of clad	0.561
Outer radius of clad	0.602

8.1 Problem 1A: single pin-cell with no IFBA

The pin-cell radial mesh is shown in Fig. 9. There are 32 angular sectors. All boundaries are reflecting.

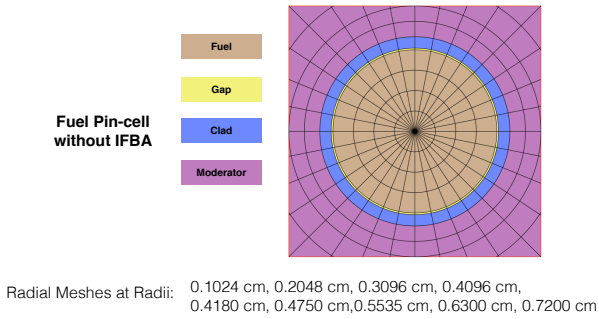

Fig. 9. The spatial mesh for pin-cell 1A

The error comparison in k-eigenvalue and collision rate versus the computational time are shown in Fig. 10. and Fig. 11. The MOC solution data points are simulated with a variety of angular quadrature sets: A4P2, A4P4, A8P4. The SN solution data points are also simulated with a variety of angular quadrature sets: S4, S8, S12, S16, S20. The dashed lines are the Monte Carlo uncertainties within two standard deviations.

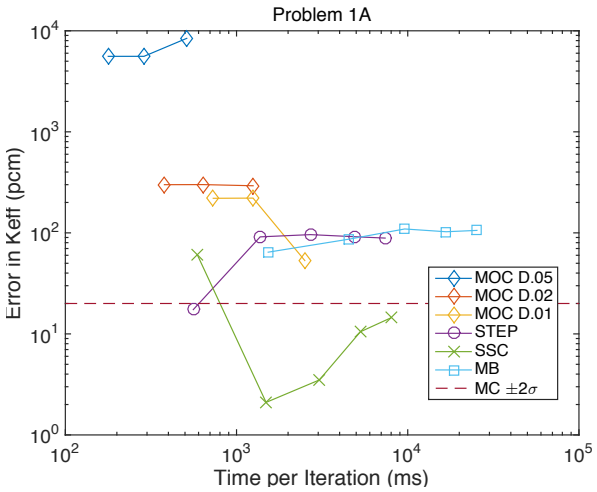

Fig. 10. K-eff error comparisons for problem 1A. The closer to the 0 the better. Data points on the same line have different quadrature sets.

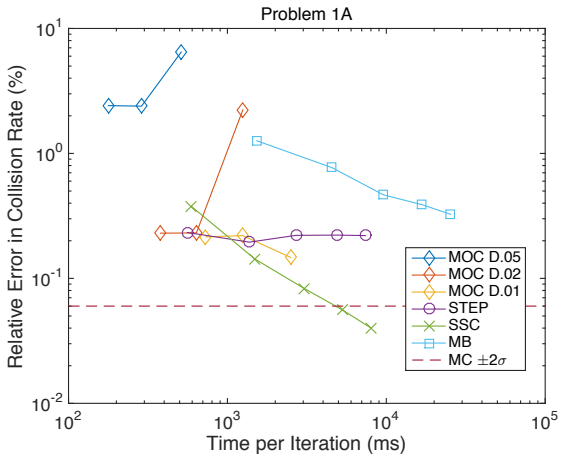

Fig. 11. Collision rate error comparisons for problem 1A. The closer to 0 the better. Data points on the same line have different quadrature sets.

When the MOC solution has a relatively wide ray spacing such as 0.05 cm and 0.02 cm, the solution do not converge when simulate with more angles. The STEP and SSC method have comparable accuracy with MOC. Table IV. compares the multigroup Monte Carlo k-effective and the KENO continuous energy Monte Carlo k-effective benchmark. We conclude that a more accurate resonance treatment is necessary to improve the solutions.

Table IV. Validation of WIMS-D Data Library for Problem 1A

Data	K-eff	K-eff Uncertainty
WIMS-D MG.	1.257067	0.000100
KENO CE.	1.183262	0.000106

8.2 Problem 1E: single pin-cell with IFBA

The pin-cell radial mesh is shown in Fig. 12. There are 32 angular sectors. All boundaries are reflecting.

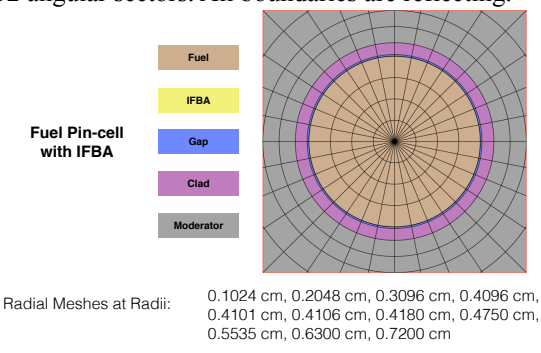

Fig. 12. The spatial mesh for pin-cell 1E

The error comparison in k-eigenvalue and collision rate versus the computational time are shown in Fig. 13. and Fig. 14. The MOC solution data points are simulated with a variety of angular quadrature sets: A4P2, A4P4, A8P4. The SN solution data points are also simulated with a variety of angular quadrature sets: S4, S8, S12, S16, S20. The dashed lines are the Monte Carlo uncertainties within two standard deviations.

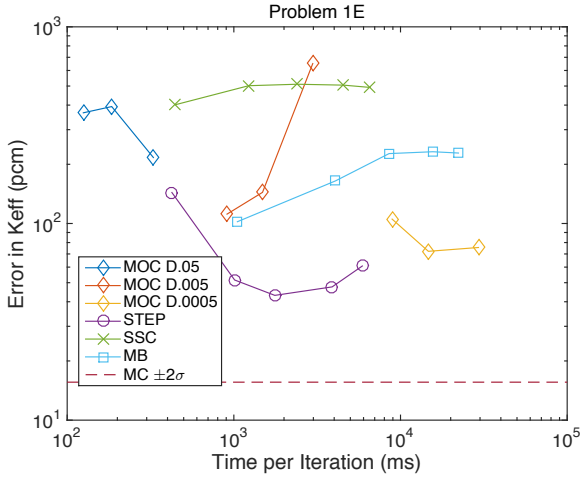

Fig. 13. K-eff error comparisons for problem 1E. The closer to 0 the better. Data points on the same line have different quadrature sets.

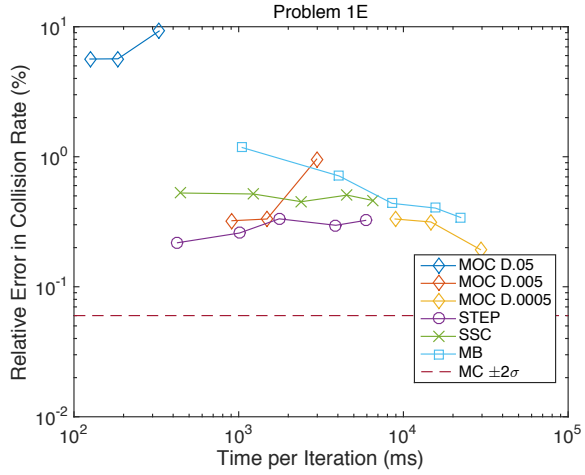

Fig. 14. Collision rate error comparisons for problem 1E. The closer to the 0 the better. Data points on the same line have different quadrature sets.

When the MOC solution has a relatively wide ray spacing such as 0.05 cm and 0.005 cm, the solution do not converge when simulate with more angles. This shows one of the advantage of SN methods when treating the very thin IFBA layer, since SN methods treat curved boundary analytically, which avoids the very fine ray spacing required by IFBA pin-cells. [12] The STEP and MB method have comparable accuracy with MOC. The SN methods i.e. STEP, SSC, and MB are less expensive than MOC with 0.0005 cm ray spacing. Table V. compares the multigroup Monte Carlo k-effective and the KENO continuous energy Monte Carlo k-effective benchmark. The WIMS-D k-effective has a large error from the continuous energy KENO benchmark, so more accurate resonance treatment is necessary.

Table V. Validation of WIMS-D Data Library for Problem 1E

Data	**K-eff**	**K-eff Uncertainty**
WIMS-D MG.	0.808911	0.000078
KENO CE.	0.772366	0.000078

Table VI. List of k-effective versus time & pin-cell power for Problem 2A

Method	Keff	Keff Error. (pcm)	Time per Iteration (ms)	Max Pin Power	Min Pin Power	Max-min Pin Power Ratio	Error in Pin Power Ratio (%)	Storage (MB)
MC (100 Million)	1.24552	4	N/A	1.0594	0.9160	1.1566	0.16	N/A
MOC A4P2 D0.05	1.24144	-407	3,913	1.0593	0.9201	1.1513	-0.46	5.467
MOC A4P4 D0.05	1.24138	-413	5,613	1.0594	0.9202	1.1513	-0.46	5.467
MOC A4P2 D0.02	1.24509	-43	8,478	1.0540	0.9185	1.1475	-0.79	13.097
MOC A4P4 D0.02	1.24503	-49	12,494	1.0599	0.9170	1.1558	-0.07	13.097
STEP S4	1.24507	-45	12,486	1.0564	0.9193	1.1490	-0.66	5.133
STEP S8	1.24403	-149	32,421	1.0556	0.9199	1.1474	-0.79	4.954
SSC S4	1.24746	194	12,837	1.0599	0.9167	1.1561	-0.04	5.133
SSC S8	1.24659	107	30,751	1.0589	0.9172	1.1545	-0.18	4.954
MB S4	1.24478	-74	23,421	1.0608	0.9161	1.1580	0.12	5.133
MB S8	1.24314	-238	58,598	1.0597	0.9168	1.1558	-0.07	4.954

8.3 Problem 2A: zero power assembly

Problem 2A is a fuel assembly contains 17x17 pin-cells, 24 of which are guide tube, one instruction tube is in the center, and the rest are fuel pin-cells. The pin-cell configuration is shown in Fig. 15. and each pin-cell is divided into 16 radial sectors. The spatial meshes are illustrated in Fig. 16, because of symmetry only a quarter is shown. All boundaries are reflecting.

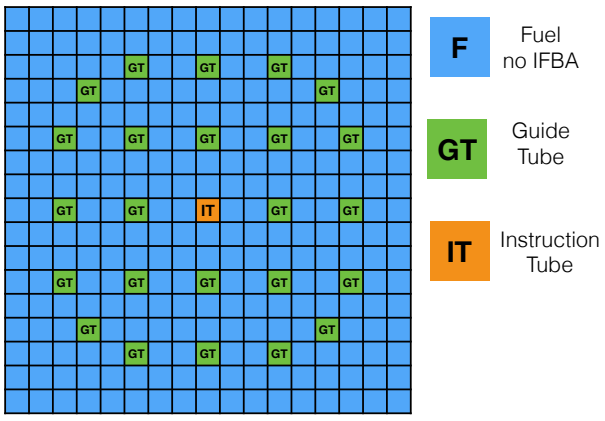

Fig. 15. The pin-cell configuration for problem 2A

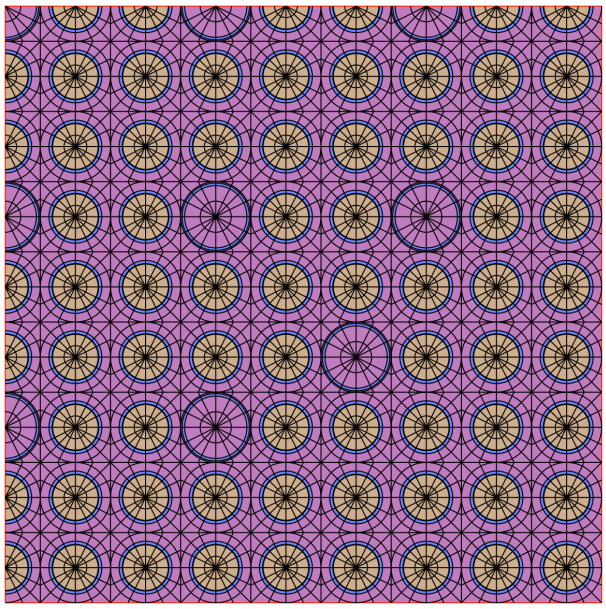

Fig. 16. The spatial mesh for problem 2A, only a quarter assembly is shown.

Table VI lists the error in k-eigenvalue, pin-cell power and the time and storage costs. The storage of the SN methods do not depend on much on the quadrature set. This is an advantage of the SN method.

The error comparison in k-eigenvalue is shown in Fig. 17. and the comparison of max-min pin power ratio is shown in Fig. 14. The MOC solution data points are simulated with two angular quadrature sets: A4P2, A4P4. The SN solution data points are also simulated with two angular quadrature sets: S4, S8. The dashed line is the Monte Carlo uncertainties within two standard deviations. The max-min pin power ratio is defined as:

$$\text{Max-min pin power ratio} = \frac{\text{Max pin power}}{\text{Min pin power}} \quad (46)$$

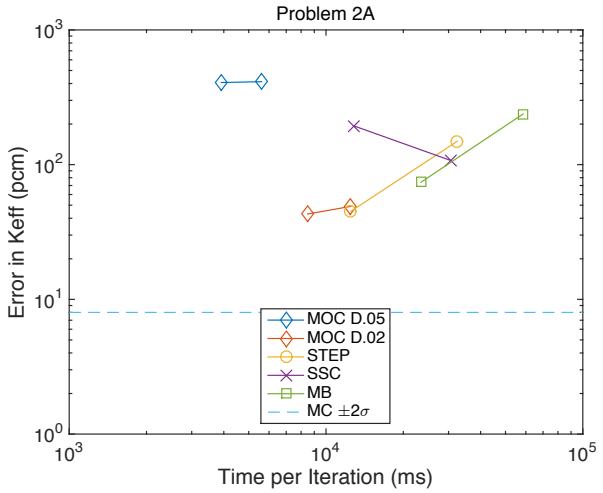

Fig. 17. K-eff error comparisons for problem 2A. The closer to 0 the better. Data points on the same line have different quadrature sets.

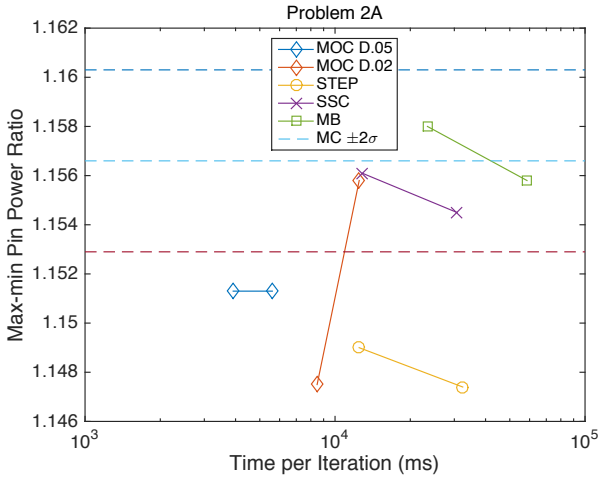

Fig. 18. Max-min pin power ratio error comparisons for problem 2A. The closer to MC dashed line the better. Data points on the same line have different quadrature sets.

In terms of k-eigenvalue, the SN method is comparable with the MOC method, and foe the max-min pin power ratio, the MB and SSC method can achieve better accuracy.

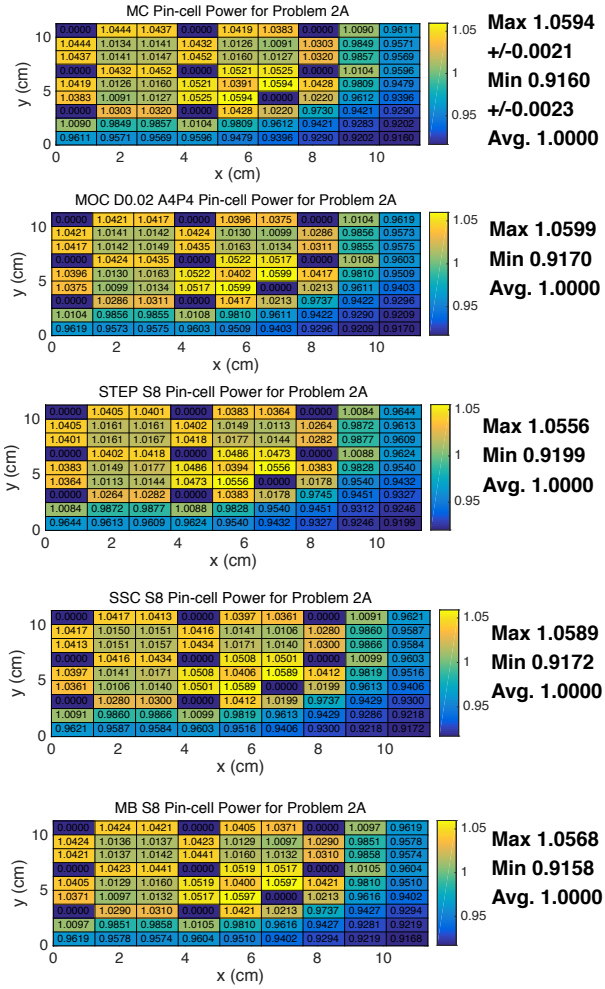

Fig. 19. Comparison of pin-cell power distribution

The pin-cell power distributions are shown in Fig. 19. and the normalization is applied such that the average is 1.0. Fig. 20. compares the relative errors in percentage to the multigroup Monte Carlo benchmark solution. The MB solution and MOC solution have comparable errors.

Table VII. compares the multigroup Monte Carlo k-effective and the KENO continuous energy Monte Carlo k-effective benchmark. Fig. 21. he multigroup Monte Carlo k-effective and the KENO continuous energy Monte Carlo pin-cell power distribution benchmark. More accurate treatment of resonance is necessary.

Table VII. Validation of WIMS-D Data Library for Problem 2A

Data	**K-eff**	**K-eff Uncertainty**
WIMS-D MG.	1.24552	0.00004
KENO CE.	1.18273	0.00002
Data	**Max Pin Power**	**Min Pin Power**
WIMS-D MG.	1.0594	0.9160
KENO CE.	1.0513	1.1191

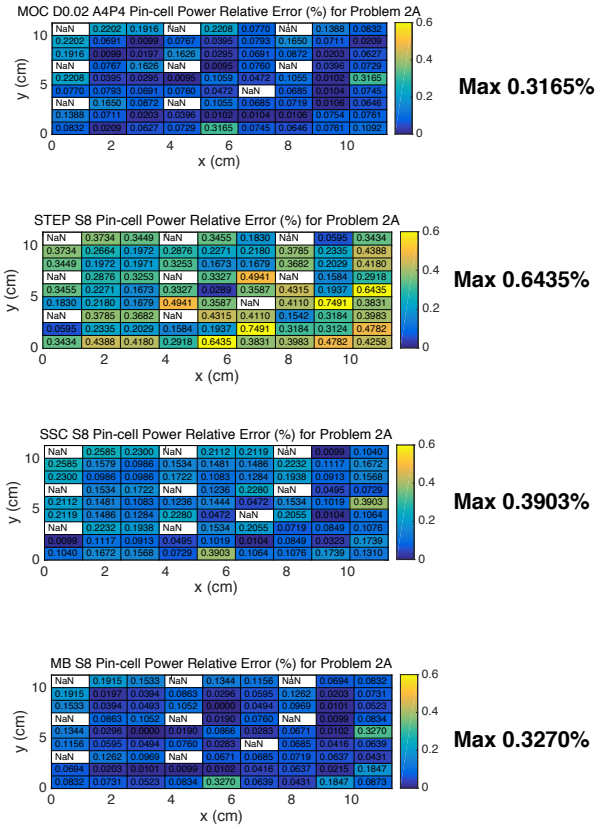

Fig. 20. Comparison of pin-cell power relative errors to the multigroup Monte Carlo benchmark solution.

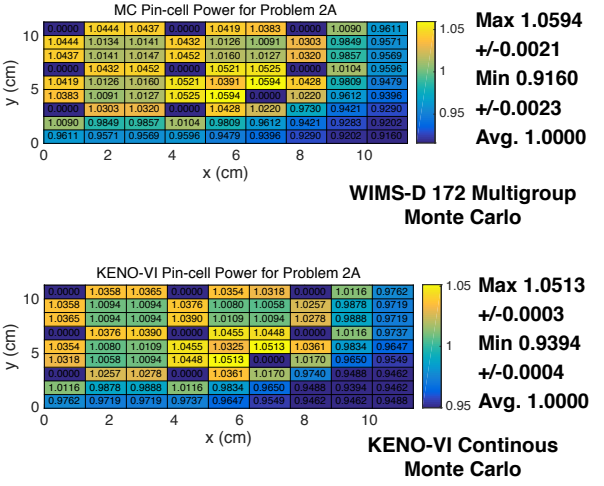

Fig. 21. Comparison between the WIMS-D mutigroup Monte Carlo and KENO-VI continuous energy pin power distribution.

9. Mini-Assembly Problem with Big Flux Gradient

We test another problem big flux gradient, which is a mini-assembly consisting of 3x3 pin-cells with vacuum boundaries surrounding the water pin-cell. Fig. 22. illustrates the geometry and spatial meshes and the material composition. The fuel pin-cells are the VERA benchmark fuel pin-cells.

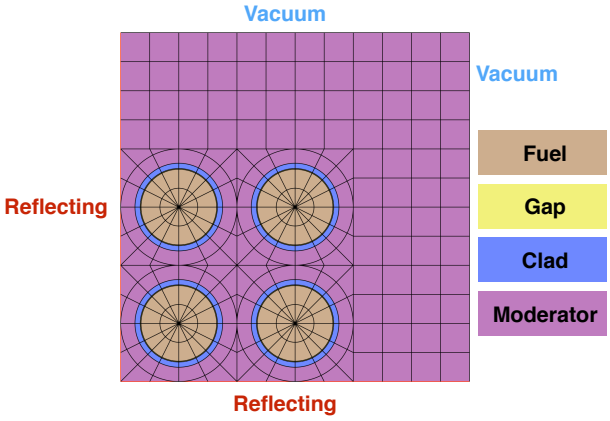

Fig. 22. The spatial grid for the mini-assembly problem, which consists of a 3x3 grid of pin-cells. The top and right boundaries next to the moderator pin-cells are vacuum, and the bottom and left boundaries next to the fuel pin-cells are reflecting.

The multigroup Monte Carlo benchmark pin-cell power distribution is shown in Fig. 23. The uncertainty is small enough so the the number is accurate within +/- 0.0001. From the center fuel pin-cell to the outer fuel pin-cell, the pin-cell power reduces by 24%. So there is a big gradient in the flux as well.

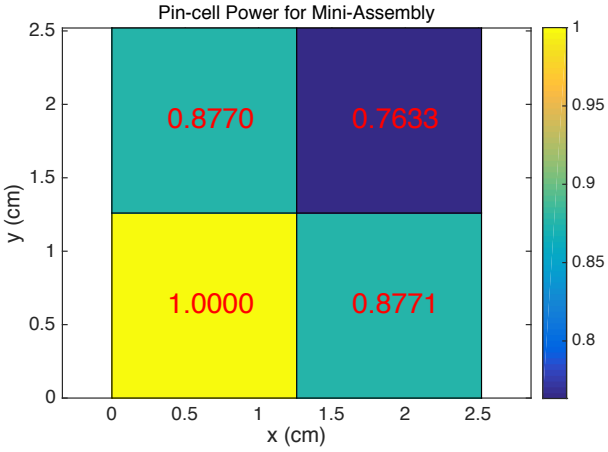

Fig. 23. The pin-cell power distribution in the fuel pin-cells.

The error comparison in k-eigenvalue is shown in Fig. 24. and the comparison of max-min pin power ratio is shown in Fig. 25. The MOC solution data points are simulated with a variety of angular quadrature sets: A4P2, A4P4, A8P4. The SN solution data points are also simulated with a variety of angular quadrature sets: S4, S8, S12, S16, S20. The dashed lines are the Monte Carlo uncertainties within two standard deviations. The max-min pin power ratio is defined in equation (46).

The MB solution is significantly better than the MOC solution. A possible reason why the MB method is the most accurate solution is because the derivation of the MB method does not assume the flux is flat in a cell, while the other methods, i.e. STEP, SSC and MOC

MOC methods all assume the flux in a cell to be flat.

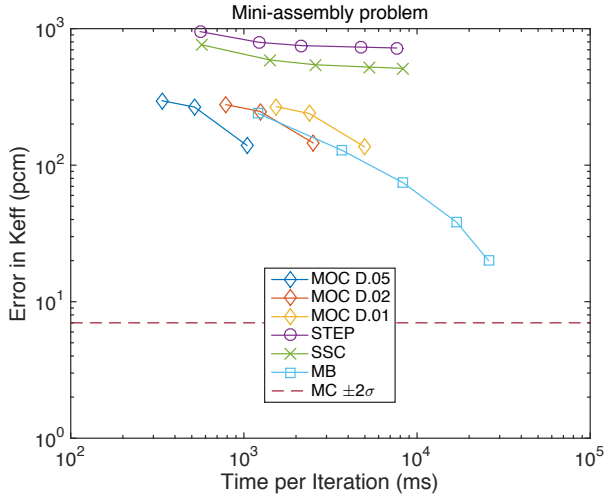

Fig. 24. K-eff error comparisons for mini-assembly problem. The closer to 0 the better. Data points on the same line have different quadrature sets.

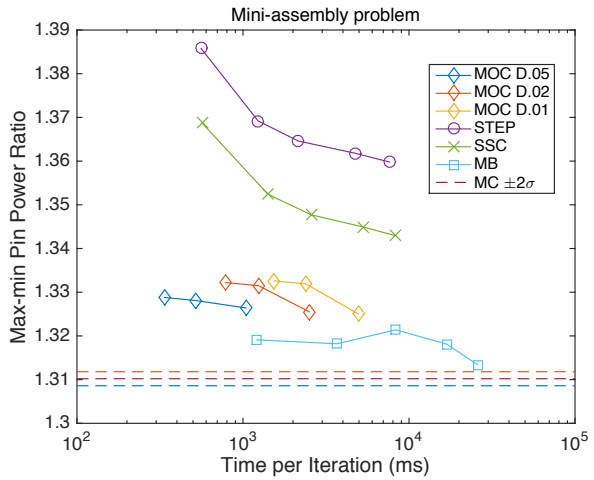

Fig. 25. Max-min pin power ratio error comparisons for the mini-assembly problem. The closer to MC dashed line the better. Data points on the same line have different quadrature sets.

10. Extension to 3-D

Extension to 3-D for the SN method discussed in the paper is straightforward, especially when the 3-D geometry is extrusion of a 2-D shapes in the axial direction (two layers with different geometries can stack together), which is frequently encountered in reactor simulation. Fig. 26. illustrates the difference between 3-D MOC and 3-D SN, where in the MOC method neutrons transport one characteristic line by one characteristic line, but in the SN method neutrons transport one layer by one layer (a layer is a 2-D plane dividing in the axial direction). The time costs for both methods are:

$$t_{moc} \propto \frac{\text{layer height}}{\text{ray spacing}} \times \#\text{ of layers} \times \text{2-D cost}, \quad (47)$$

$$t_{sn} \propto \#\text{ of layers} \times \text{2-D cost}. \quad (48)$$

For MOC the information of each characteristic line is required to store, the storage costs for both methods are:

$$s_{moc} \propto \frac{\text{layer height}}{\text{ray spacing}} \times \#\text{ of layers} \times \text{2-D cost}, \quad (49)$$

$$s_{sn} \propto \#\text{ of layers} \times \text{2-D cost}. \quad (50)$$

When all layers have the same geometry, only one 2-D plane information is required to store. A recent work conducted at MIT aims at reducing the MOC storage cost to be close to $\propto \#\text{ of layers} \times \text{2-D cost}$ [2].

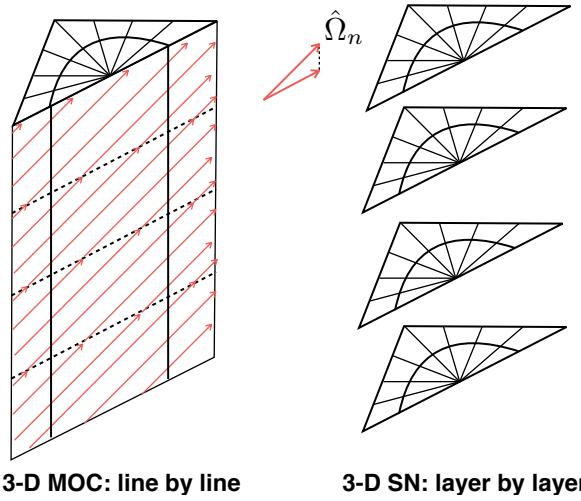

Fig. 26. Illustration of the difference between 3-D MOC and 3-D SN transport.

We saw from numerical results that MOC and SN have comparable time and storage cost. So when extended to 3-D, SN methods are advantageous over the MOC method in terms of time and storage cost.

11. Conclusion

In conclusion, we have studied realistic problems from a simple pin-cell to an assembly, using an industrial standard cross section library. We demonstrate that the discrete ordinates methods including STEP, SSC and MB can be an alternative method to MOC for reactor simulation.

We find that the SSC and MB methods are comparable to MOC in both accuracy and computational cost. For difficult problems with large spatial flux gradients, our simulations show that the MB method is significantly more accurate.

Moreover, given the widely-acknowledged inability of MOC to realistically treat 3-D geometries, it seems highly likely that for 3-D problems, the SN methods will be considerably more efficient than MOC.

Acknowledgements

Thanks to Prof. Joo, Hangyu from Seoul National University for coordinating the RPHA15 meeting and offering an opportunity for submitting this paper. The invitation from Prof. Shaohong Zhang from Shanghai NuStar Corporation to the RPHA15 is greatly appreciated. Ms. Yu, Hui, Li, Shou and Liu, Zhiyan from SNPSDC, Beijing inspire this paper of using the WIMS-D data library to study the VERA benchmark problems. Boyd, Will, Ms. Li, Lulu from MIT, Prof. Wang, Kan from Tsinghua University, and Cao, Liangzhi from Xi'an Jiaotong University also gave feedback to the some related work. Without the long lasting help from Prof. Larsen, Edward, Downar, Thomas, Marin, William, and my graduate colleagues Liu, Yuxuan and Zhu, Ang from University of Michigan, this work is not possible. The encourage from the deputy vice president Lin, Zhongqin from Shanghai Jiaotong University, Ms. Yang, Yanhua and Chen, Yixue from SNPSDC Beijing are highly appreciated. Finally, special thanks to the vice executive officer Liu, Zhaohua from CNNC Tianwan Nuclear Power Plant for giving me my first touch with the nuclear industry.

References

1. Godfrey, A. "Vera Core Physics Benchmark Progression Problem Specifications," CASL-U-2012-0131-004 (2014).
2. Gunow, Geoffrey, John Tramm, Benoit Forget, and Kord Smith, Tim He, "SimpleMOC - A Performance Abstraction for 3D MOC," *Proc. ANS MC2015,* Nashville, TN, April 19–23, 2015, American Nuclear Society (2015) (CD-ROM).
3. Hebert, A. "Applied Reactor Physics", Presses Internationales Polytechnique, Canada (2009).
4. Hyun, Min Ryu, Ho Cho, Chang Hyun Lim, Yeon Sang Jung and Han Gyu Joo, "Preliminary Assessment of nTRACER and McCARD Direct Whole Core Transport Solutions to VERA Core Physics Benchmark Problems", Transactions of the American Nuclear Society, Anaheim, California, Nov. 09–13, 2014, CD-ROM(2014)
5. Leszczynski, F. D. L. Aldama, and A. Trkov, "WIMS-D Library Update," International Atomic Energy Agency, Vienna, Austria (2007).
6. Liu, Changyuan, Ph.D. Thesis:, Discrete Ordinates Methods for Curved Spatial Grids, University of Michigan (2015).
7. Liu, Yuxuan, Ph.D. Thesis: A Full Core Resonance Self-shielding Method Accounting for Temperature-dependent Fuel Subregions and Resonance Interference, University of Michigan (2015).
8. Lucas, D.S., 'Core Modeling of the Advanced Test Reactor with the Attila Code', M&C 2005: International Topical Meeting on Mathematics and Computation, Supercomputing, Reactor Physics, and Nuclear and Biological Applications, Avignon, France (2005).
9. Marleau, G., Hebert, A., Roy, R., A User Guide for DRAGON Version 4, IGE-294, Institut de genie nucleaire, Ecole Polytechnique de Montreal (2013).
10. Morel, J.E. and Larsen, E. "A Multiple Balance Approach for Differencing the SN Equations," Nuc. Sci.and Eng. **105**, 1-15 (1990).
11. MPACT Development Team, "MPACT User Manual," University of Michigan, Ann Arbor, (2013).
12. Walker, D. Erik, M.S. Thesis: Modeling Integral Fuel Burnable Absorbers Using the Method of Characteristics, University of Tennessee (2014).